Mechanics of beams made from chiral metamaterials: Tuning deflections through normal-shear strain couplings

Mechanics of beams made from chiral metamaterials: Tuning deflections through normal-shear strain couplings

N. Karathanasopoulos [a,*], F. Dos Reis [b], M. Diamantopoulou [a], J.-F. Ganghoffer [b]

[a] Chair of Computational Modeling of Materials in Manufacturing, Department of Mechanical and Process Engineering, ETH, Zurich, Switzerland
[b] LEM3, CNRS/Université de Lorraine, Metz, France

HIGHLIGHTS

- The mechanics of chiral beams with inner normal-shear strain couplings is elaborated, starting from first principles.
- Normal deformations create bending deflections which are proportional to the material's shear-normal compliance coefficient.
- The use of inner strain couplings as an equilibration mechanism is numerically and experimentally tested for the first time.
- The bending deflections' equilibrating force is inversely proportional to the material's shear-normal coupling coefficient.

GRAPHICAL ABSTRACT
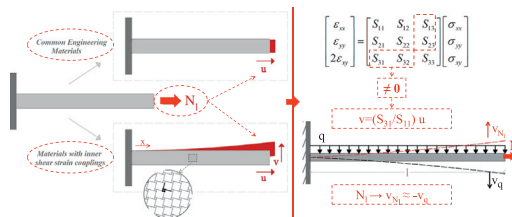
ABSTRACT

In the current work, we demonstrate the potential of structures made of chiral artificial materials to balance bending loads through tensile loads, exploiting their inner normal to shear strain coupling. To that scope, we employ beam structures which we architecture with tetrachiral unit-cells. For the latter, we quantify their inherently coupled normal to shear strain behavior, making use of homogenization analysis techniques. We subsequently derive the equations that characterize the bending mechanics of beams with an inner bending to normal loading coupling, starting from first principles. Thereupon, we compute the normal forces required to equilibrate the effect of bending loads on beam structures, providing relevant closed-form parametric expressions. Using the derived analytical formulas, we carry out both numerical simulations and experiments for the case of cantilever beams. Results suggest that the coupling of normal and shear deformations can be used as a primal load-balancing mechanism, providing new possibilities in the control of the artificial structure's kinematics and overall mechanics.

© 2020 The Authors. Published by Elsevier Ltd. This is an open access article under the CC BY-NC-ND license (http://creativecommons.org/licenses/by-nc-nd/4.0/).

1. Introduction

During the last decades, a new paradigm has been developed in the design of materials, in which the material's macroscale properties are designed through the appropriate organization of its inner structure [1]. A new class of artificial materials appeared, that have been commonly named as metamaterials [2]. Metamaterials are typically based on periodic unit-cell arrangements [3], engineered to a μm accuracy scale thanks to the emergence and development of additive manufacturing [4,5]. A basic cell is used as the repetitive material unit, substituting the notion of atoms in conventional materials [6].

For the static or dynamic structural material attributes to be obtained, experimental or numerical studies need to be carried out [7–9]. The latter can be considerably computationally expensive, if full-scale finite element models are employed [10]. A link between the metamaterial's inner architecture and its equivalent continuum scale properties can be derived using homogenization analysis methods [11,12]. Such methods have been primarily based on asymptotic expansion techniques for the static and kinematic variables of the metamaterial's inner unit-cell architecture [13]. Discrete homogenization methods allow for a complete characterization of the continuum-scale compliance matrix, providing closed-form, parametric expressions for each stiffness component [14].

The design of a wide range of unit-cells has been up to now directed by the effective volumetric behavior of the arising continuum, quantified by the Poisson's ratio values. The latter has been long considered to be a fundamental metric of material performance [15]. Within isotropy, the material's normal and shear modulus are directly and uniquely related to its effective Poisson ratio value ν, so that a negative Poisson ratio value entails an increased shear stiffness ($G = E/(2(1 + \nu))$) [16]. The observation gave birth to a class of artificial materials, named as auxetics, as they laterally expand rather than contract when normally stretched, contrary to most common engineering materials [17–19]. Well-known lattice architectures with an auxetic mechanical behavior are the so-called re-entrant type unit-cell designs, such as re-entrant hexagonal or star-shaped lattices [20–24]. Apart from auxetic unit-cell designs, lattice configurations that oppose lateral expansion upon normal loading have been devised [25,26]. Representative unit-cells of the kind are rectangular-shaped lattices or combinations of re-entrant hexagonal with regular hexagonal lattice architectures, named as semi-re-entrant structures [26,27]. Moreover, several lattice configurations with a positive Poisson's ratio that is comparable to the one of common engineering materials have been reported, typical examples being honeycomb, kagome or triangular-shaped unit-cell architectures [26,28].

Artificial materials have been engineered so as to meet, not only certain effective volumetric behaviors, but primarily to satisfy flexibility and weight requirements [29–31]. In particular, lightweight materials with prescribed structural characteristics constitute primal objectives in different engineering fields, among others in morphing and composite engineering [32]. Within isotropy, the range of attainable effective material properties lies within rather confined limits, so that anisotropic material architectures are required to broaden the feasible design space [33]. In such a space, the material's normal and shear resistance can be tuned independently from other primal material parameters, such as from the material's effective Poisson ratio value [34]. Up to now, different anisotropic unit-cell designs with ultra-soft or ultra-stiff effective normal material resistance have been contrived [35–37]. Their normal modulus can be controlled to substantially vary among the different material loading directions, exceeding the isotropic limits by orders of magnitude [38,39].

The inner material architecture and the degree of anisotropy of architected media affect, not only their static, but also their wave-propagation characteristics. More specifically, dispersion attributes well differ between isotropic, hexagonal-shaped lattices and anisotropic, auxetic inner material architectures [40–43]. What is more, stiffness anisotropy can be exploited to provide wave propagation isolation features, both for normal and shear waves [39]. Anisotropic inner mass density distributions can be as well used to manipulate longitudinal [44] and flexural [45] waves over certain frequency regions. Such inner material designs form the basis for the engineering of devices with focusing and subwavelength imaging capabilities; attributes of primal importance in the field of non-destructive structural evaluation [46].

Most of the previously reported effective mechanical properties arise from inner material designs whose effective bulk deformation is uncoupled from rotations [47,48]. As such, when compressed or tensioned, they simply normally deform, without changing their shape

(Fig. 1). However, this is not uniquely the case for a specific class of metamaterials which have been named as chiral due to their inherent lack of symmetry with respect to their mirror lattice image [49,50]. Up to now, different chiral lattice designs have been reported, yielding either isotropic auxetic –as for hexachiral lattices [51]- or anisotropic and non-auxetic effective material behaviors, as in the case of chiral-diamond and tetrachiral lattices [52,53]. For the latter, bulk deformations are coupled to rotations creating a normal to shear strain coupling, already at the constitutive level [53]. This inherent coupling leads to a macroscopic response where normal forces induce shear-forces and vice-versa, so that normal loads induce lateral deformations, as schematically depicted in Fig. 1.

Lateral bending deformations as of the application of normal forces have been artificially created with the use of additional structural elements, such as cables. The latter constitute common practice in the case of structures, for which some load equilibration mechanism needs to be applied to counterbalance bending deflections, with typical macroscale examples being bridge structures [54]. For such systems, the additional element needs to be eccentrically placed and normally pre-stressed to create inner moments and shearing forces that cancel out the bending loading pattern of interest [54,55]. However, the use of advanced materials with an inner coupling of normal and bending deformations premises a bending equilibration functionality, which arises from the material's very constitutive behavior and not from the use of additional elements; a potential that has not been up to now studied. What is more, the relation between bending and normal deformations remains unknown, along with the constitutive formulation of the effective macroscale forces and moments.

In the current work, we investigate the potential of artificial materials to equilibrate bending deformations through tensile loads out of their constitutive behavior. To that scope, we make use of tetrachiral unit-cell structures that lead to a macroscopic, homogenized response with an inherent normal to shear strain coupling. We introduce the artificial material's architecture and basic constitutive relations in Section 2. Thereafter, we derive the bending equilibrium equations of beam elements for the case of materials with an inherent normal to shear strain coupling, starting from the full order compliance matrix (Section 3.1). In Section 3.2, we summarize the numerical specifications of a cantilever beam architectured with tetrachiral lattices, while in Section 4 we elaborate the experimental fabrication and testing procedures of micro-architectured tetrachiral cantilever beams. In Section 5, after summarizing the effective mechanical properties of the tetrachiral lattice (Section 5.1), we provide the deformation and equilibrium mechanics of cantilever beam structures with inner normal to shear strain couplings (Section 5.2). We make use of the obtained results to equilibrate the end tip deflection of a deflected beam structure through tension (Section 5.3), while we analyze both analytically and experimentally the normal-load induced, bending kinematics (Section 5.4). We provide an overall discussion on the implications of the coupling between bulk and shear deformations in Section 5.5 and conclude in Section 6.

2. Materials and methods

2.1. Metamaterial architecture

Among typical chiral lattice structures [49,51,52], we select the tetrachiral lattice structure for the present work as a typical anisotropic unit-cell design with an inherent normal to shear strain coupling. Fig. 2 shows a schematic of the lattice structure along with a detailed view of its unit cell. The nodes of the primal unit-cell are represented with filled black circles, while its periodicity vectors λ_1, λ_2 in red. In a first approximation, the relative density ρ^* of the two-dimensional structure with elements of thickness t and length L are expressed as a function of
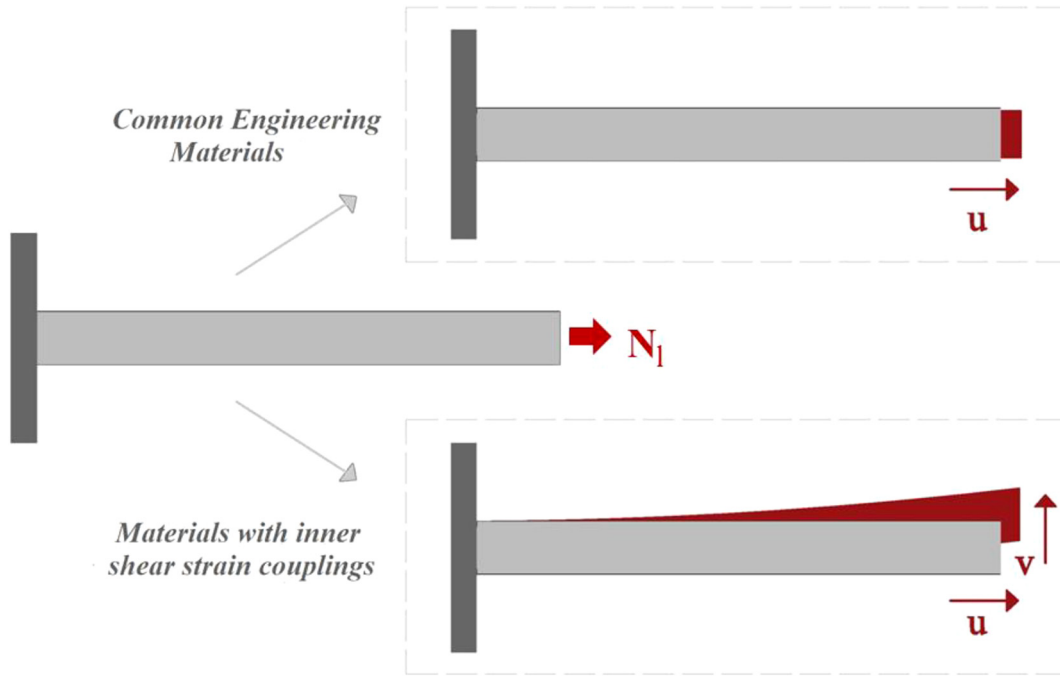
Fig. 1. Schematic representation of the deformation mechanism for a common engineering material and for a material with an inner normal to shear strain coupling.

their slenderness $\eta = L/t$ and angle θ, as follows:

$$\rho^* = 2(s + c)/\eta \tag{1}$$

where s and c in Eq. (1) stand accordingly for $\sin\theta$ and $\cos\theta$. Fig. 3a depicts the dependence of the unit-cell architecture on the angle θ, while Fig. 3b provides the relative density ρ^* for different values of the slenderness ratio η and lattice angle θ.

The structure is of chiral nature so that its mirror image is different from the structure itself [49]. This lack of mirror symmetry is responsible for an unconventional mechanical response, as shown in the sequel. Different from most engineering materials, no in-plane direction can be found for which the application of normal stresses does not induce any shear deformation. In other words, the normal and shear deformations are coupled in the tetrachiral lattice, which will be mathematically

detailed and exploited at the structural level in the developments to follow.

2.2. Constitutive relations

The elastic constitutive equations are developed for describing the macroscopic stress-strain response of tetrachiral metamaterials for plane stress conditions, i.e. for conditions where the structure can deform freely along the out-of-plane direction. For a general anisotropic solid, the elastic stress-strain relationship may be written in the following form:

$$\boldsymbol{\varepsilon} = \mathbf{S}\boldsymbol{\sigma} \rightarrow \begin{bmatrix} \varepsilon_{xx} \\ \varepsilon_{yy} \\ 2\varepsilon_{xy} \end{bmatrix} = \begin{bmatrix} S_{11} & S_{12} & S_{13} \\ S_{21} & S_{22} & S_{23} \\ S_{31} & S_{32} & S_{33} \end{bmatrix} \begin{bmatrix} \sigma_{xx} \\ \sigma_{yy} \\ \sigma_{xy} \end{bmatrix} \tag{2}$$
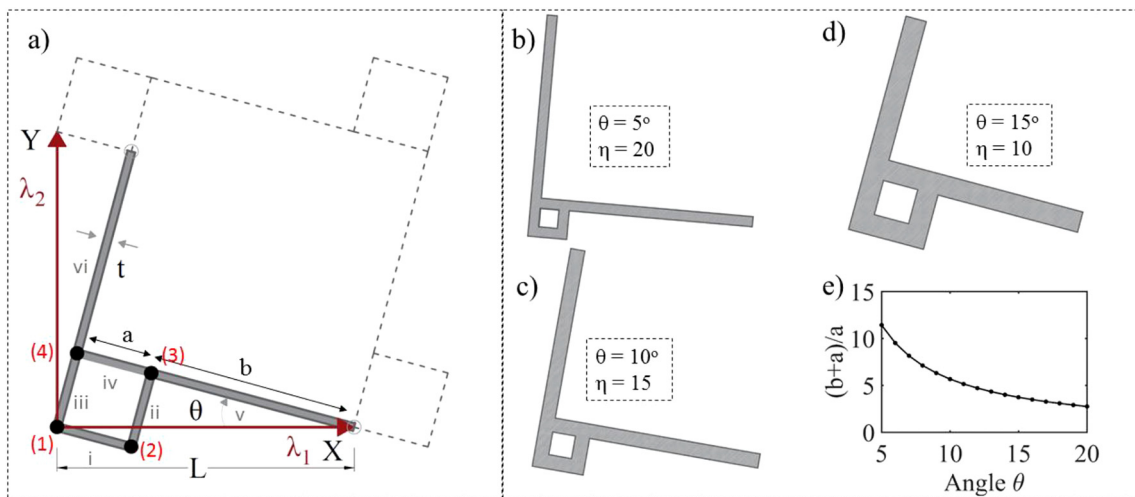
Fig. 2. Tetrachiral-shaped unit-cell along with its periodicity in dashed lines. The unit-cell internal nodes are denoted with red, while the numbering of the unit-cell's beam elements with latin characters (a). Different realizations of the unit-cell structures are provided in (b)-(d) for varying lattice angles θ and slenderness ratio values η. The ratio of the total arm length to the square side length $(a + b)/a$ is provided as a function of the lattice angle θ in (e). (For interpretation of the references to colour in this figure legend, the reader is referred to the web version of this article.)

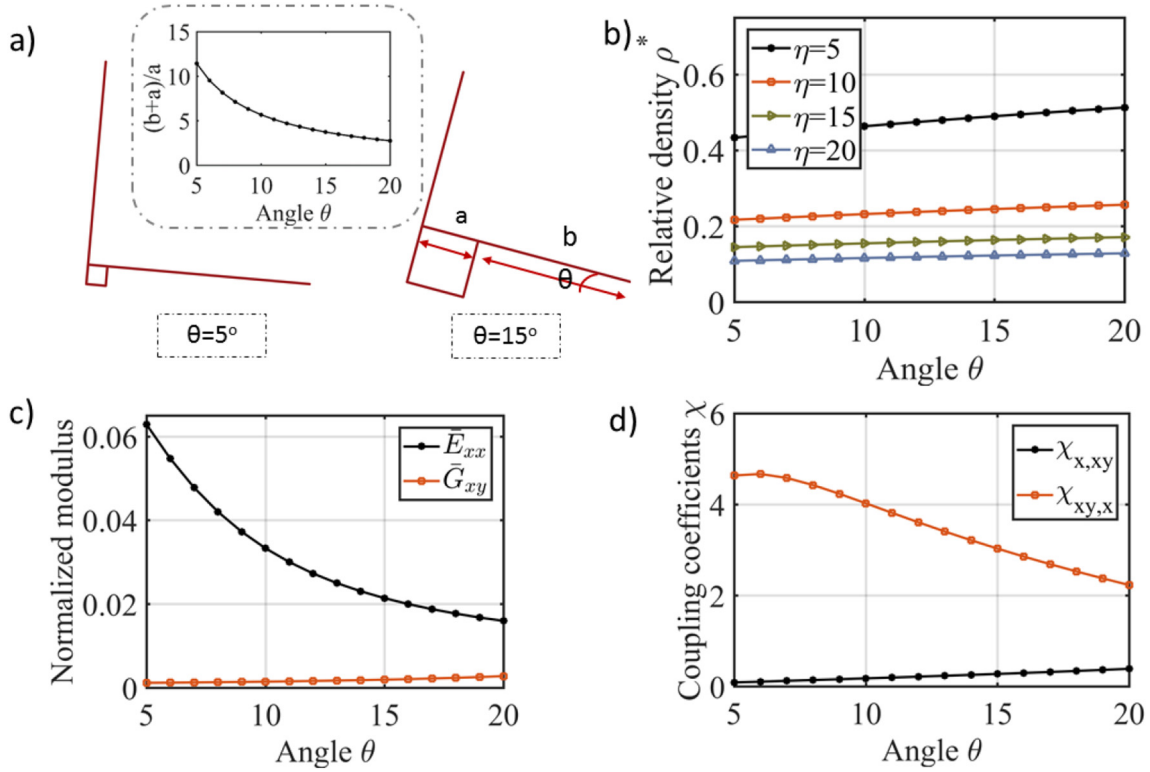**Fig. 3.** Tetrachiral lattice geometry as a function of the angle θ (a). The relative density evolution for different lattice angles θ and element slenderness ratios η (b). Normal and shear modulus evolution as a function of θ for a lattice with $\eta = 10$ normalized with respect to the elastic modulus of the basis material (c). The dependence of the coupling coefficients on the parameter θ for a lattice with a slenderness $\eta = 10$ (d).

where ε_{xx}, ε_{yy} denote the normal strain components and ε_{xy} the mathematical shear strain in an x-y-coordinate frame (small strain setting). The corresponding Cauchy stress components are denoted as σ_{xx}, σ_{yy} and σ_{xy}. The relationships among the six independent components of the symmetric compliance tensor (in the x-y-coordinate system) and the elastic normal and shear moduli, as well as the Poisson's ratios read [33]:

$$E_x = \frac{1}{S_{11}}, E_y = \frac{1}{S_{22}}, G_{xy} = \frac{1}{S_{33}}, \ \nu_{yx} = -\frac{S_{12}}{S_{22}}, \nu_{xy} = -\frac{S_{21}}{S_{11}} \tag{3}$$

We define the non-dimensional normal to shear $\chi_{x,xy}, \chi_{y,xy}$ and shear to normal coupling coefficients $\chi_{xy,x}, \chi_{xy,y}$, by dividing with respect to the shear (S_{33}) and normal (S_{11}, S_{22}) compliance-related terms, as follows:

$$\chi_{x,xy} = \frac{S_{13}}{S_{33}}, \chi_{y,xy} = \frac{S_{23}}{S_{33}}, \chi_{xy,x} = \frac{S_{31}}{S_{11}}, \chi_{xy,y} = \frac{S_{32}}{S_{22}} \tag{4}$$

Using the definitions of Eqs. (3) and (4), the compliance tensor **S** of Eq. (1) is written as follows:

$$\mathbf{S} = \begin{bmatrix} \dfrac{1}{E_x} & \dfrac{-\nu_{yx}}{E_y} & \dfrac{\chi_{x,xy}}{G_{xy}} \\ \dfrac{-\nu_{xy}}{E_x} & \dfrac{1}{E_y} & \dfrac{\chi_{y,xy}}{G_{xy}} \\ \dfrac{\chi_{xy,x}}{E_x} & \dfrac{\chi_{xy,y}}{E_y} & \dfrac{1}{G_{xy}} \end{bmatrix} \tag{5}$$

The components of the material's stiffness tensor **C** (in the x-y coordinate system) are obtained by inverting the compliance matrix $\mathbf{C} = \mathbf{S}^{-1}$.

2.3. Models for computing the constitutive response

2.3.1. Discrete homogenization analysis

We compute the lattice effective mechanical properties using a discrete homogenization analysis technique. As detailed in [13,14], the stiffness matrix **C** is obtained through the Riemann integral of the stress vector contributions $\mathbf{S}^i$ of each node over the unit-cell.

$$\int_\Omega \boldsymbol{\sigma} \frac{\partial \mathbf{v}_f}{\partial x} dx = 0, \ \ \boldsymbol{\sigma} = \frac{1}{g} \mathbf{S}^i \otimes \frac{\partial R}{\partial \lambda^i}, \mathbf{S}^i = \sum_{b\in\Omega} \mathbf{F}^b \delta^{ib} \tag{6}$$

In Eq. (6), $\mathbf{F}^b$ stands for the normal and transverse forces in each inner lattice element, while R for the position vectors of the lattice inner nodes as defined by the periodicity vectors λ^i of the unit (Fig. 2) andgfor the Jacobian of their transformation to the Cartesian system$X$, Y. The parameter δ^{ib} describes the tessellation of the unit-cell, taking values in the subset $\delta^{ib} \in [-1, 0, 1]$. The stress-vector contributions $\mathbf{S}^i$ in Eq. (6) are determined from the asymptotic expansion form of the equilibrium equations over the lattice geometry. The asymptotic expansion is carried out both for the static and kinematic variables, while the overall equilibrium writes:

$$\begin{aligned} \sum_{v\in Z^2} \sum_{b\in\Omega} \mathbf{F}^b \big(\mathbf{v}_f(O) - \mathbf{v}_f(E)\big) = 0 \\ \sum_{v\in Z^2} \sum_{b\in\Omega} \mathbf{M}^O \mathbf{w}(O) + \mathbf{M}^E \mathbf{w}(E) = 0 \end{aligned} \tag{7}$$

where in Eq. (7), $\mathbf{v}_f(O)$, $\mathbf{w}(O)$ and $\mathbf{v}_f(E)$, $\mathbf{w}(E)$ represent accordingly the velocity and rotation fields and $\mathbf{M}^O, \mathbf{M}^E$ the moments developed at the origin and extremity of each inner unit-cell element. We provide the complete tessellation of the structure entering the equilibrium equations of Eq. (7) in Table 1, following the nodal and element numbering of Fig. 1a.

2.3.2. Finite element homogenization analysis

For validation purposes, we compare the discrete homogenization results with full-scale finite element models comprised of 11 tetrachiral cells in each material direction. The unit-cells follow an angle of $\theta = 15°$ while models of different slenderness are constructed by varying the thickness of its arms, so that η takes discrete values between 5 and 30, upon increments of 5. Compliance-based moduli verifications are carried out, applying normal and shear stresses (Eq. (2)). For the normal stress application, the models are constrained in the middle of their left side and deformed at their right side along the X direction, upon a free lateral contraction. For the shear tests, the left side of the models is constrained and a stress along the Y axis is applied at their right side. In each case, the elastic modulus E_x, the coupling coefficients $\chi_{xy, x}$, the shear modulus G_{xy} and the coefficient $\chi_{x,xy}$ are obtained, using the definitions of Eqs. (3)–(4).

3. Structural analysis

To demonstrate the unconventional mechanical response of chiral metamaterials at the structural level, the mechanical response of a cantilever beam made from the above tetrachiral metamaterial is analysed in detail. For this, we develop an extended Timoshenko beam theory (Section 3.1), as well as a detailed finite element model of a cantilever beam with a tetrachiral mesostructure (Section 3.2).

3.1. Extended Timoshenko beam theory

We start with the standard kinematics of the Timoshenko beam theory [56]. For the two-dimensional, small strain case, with no axial twist moment development ϕ_x and zero out of plane deformations ($\theta_y = 0$), the motion of the beam centerline [57] is described through the axial displacement $u(x)$ and the deflection $v(x)$, as depicted in Fig. 4. The displacement of a point with coordinates (x, y) comprised within the beam then reads:

$$u_x(x,y) = u(x) - y\theta_z(x) \tag{8}$$

$$u_y(x,y) = v(x)$$

where θ_z in Eq. (8) denotes the rotation of beam cross-section around the z-axis (Fig. 4). According to the previously defined kinematics, we compute the normal strain field component:

$$\varepsilon_{xx} = \frac{\partial u(x,y)}{\partial x} = \frac{\partial}{\partial x}(u(x) - y\theta_z(x)) = u'(x) - y\theta'_z(x), \tag{9}$$

and the shear strain field component, as follows:

$$2\varepsilon_{xy} = \frac{\partial u(x,y)}{\partial y} + \frac{\partial v(x,y)}{\partial x} = \underbrace{-\theta_z + v'(x)}_{=\overline{\gamma}_y} \tag{10}$$

After inserting the stress-strain relations for a fully anisotropic material (Eq. (2)), we have:

$$S_{11}\sigma_{xx} + S_{12}\sigma_{yy} + S_{13}\sigma_{xy} = u'(x) - y\theta'_z(x), \tag{11}$$

Table 1
Tessellation of the tetrachiral lattice unit-cell architecture of Fig. 2a.

Beam (b)	i	ii	iii	iv	v	vi
O (b)	1	2	1	3	3	4
E (b)	2	3	4	4	1	2
δ_1	0	0	0	0	1	0
δ_2	0	0	0	0	0	1

$$S_{31}\sigma_{xx} + S_{32}\sigma_{yy} + S_{33}\sigma_{xy} = \underbrace{-\theta_z + v'(x)}_{=\overline{\gamma}_y}. \tag{12}$$

Next, we integrate both the left and right hand sides of Eqs. (11) and (12) over the cross-sectional area A. We neglect the normal stress term in the y-direction and introduce the generalized forces $N(x) = \int \sigma_{xx}dA$ (axial force), $V(x) = \int \sigma_{xy}dA$ (shear force), and $M_z(x) = \int -y\sigma_{xx}dA$ (bending moment) [57]. The resulting normal and shear force equilibrium equations then reads:

$$S_{11}N + S_{13}V = u'(x)A - \theta'_z(x)\underbrace{\int_A ydA}_{=0}, \tag{13}$$

$$S_{31}N(x) + S_{33}V(x) = (-\theta_z + v'(x))A \tag{14}$$

The final expressions for the generalized axial and shear forces are then obtained after substituting the compliances by the corresponding moduli (Eq. (3)), as follows:

$$N(x) = E_xAu'(x) - \frac{S_{13}}{S_{11}}V(x) \tag{15}$$

$$V(x) = G_{xy}A(-\theta_z + v'(x)) - \frac{S_{31}}{S_{33}}N(x) \tag{16}$$

In close analogy, an explicit expression for the bending moment is obtained, when multiplying Eq. (11) with y before integration:

$$M_z(x) = \theta'_z(x)E_xI_z \tag{17}$$

with $I_z = \int y^2dA$ denoting the second moment of inertia. Eqs. (15)–(17) define a set of differential equations for the functions $u(x)$, $v(x)$ and $\theta_z(x)$. In the case of statically-determinate systems, the generalized forces are known from equilibrium and the solutions for $u(x)$, $v(x)$ and $\theta_z(x)$ are readily obtained through integration.

3.2. Detailed cantilever beam finite element model

In order to numerically study the mechanics of beams architected with materials with a fully anisotropic constitutive behavior, we construct a beam structure with a length of 222 mm and a height of 55 mm, architected with 30 cells along its length and 8 cells along its width, as schematically depicted in Fig. 7a. The tetrachiral cells follow an angle of $\theta = 15°$ and are given a slenderness ratio of $\eta = 10$. The modulus of the basis material is $E_s = 200\,GPa$, while the out of $x - y$ plane thickness is 0.84 mm. The cantilever structure is held fixed at its left end, while a normal force N_l is applied at its right end, as schematically depicted in Fig. 7. The structure is discretized with standard linear solid elements with a fine enough refinement of approximately 10 solid elements for each of the arms of the tetrachiral lattice (Fig. 7a).

4. Experimental procedures

We complement the analytical formulations and numerical models by experiments. In the current section, we detail the fabrication process and the experimental setup of a micro-architectured cantilever beam.

4.1. Fabrication

Micro-architectured cantilever beam structures are fabricated with the use of a two-photon polymerization technique via a direct laser writing system provided by Nanoscribe GmbH (Photonic Professional GT). The structures of approximate dimensions of 180 μm × 200 μm × 600 μm (cross section and length respectively,

Fig. 8) are written on glass substrates with the use of the IP-S photoresist and the dip-in mode with a laser power of 40 mW and scan speed of 10 mm s^{-1}. For the development process, the structures were dipped in a developer solution (Mr Dev 600) for 12 min and in isopropyl alcohol bath for another 2 min. Nitrogen gas was used for drying the samples after the development process was completed.

4.2. Microstructure imaging

The micro-chiral structures were observed with a Scanning Electron Microscope (SEM) by FEI (Scios, Dual Beam). From the images captured, the length, width and height of the specimens were measured, as well as the feature sizes like wall thickness and the inner tetrachiral arm length (Fig. 8a). Based on the measurements made, the slenderness ratio of the tetrachiral cells was computed to be $\eta = 6.5 \pm 0.5$, with the variation to be attributed to imperfections during the polymerization and solvation process.

4.3. Compression testing

Uniaxial compression experiments were conducted in order to obtain the displacement profile of the structures, as schematically represented in Fig. 4. A custom-made displacement-controlled microtesting device was used for the purpose of this study [58]; the device features a 5-axis stage on which the glass substrate with the micro-chiral structures is attached. The structures were aligned and compressed against a flat punch of 1 mm × 0.5 mm dimensions that is connected to a strain-gaged load cell by Omega (LCAE 6 N). The flat punch was moved by a piezolegs motor (Micromo, model LEGS Linear Twin 40 N) at a prescribed speed of 1 μm s^{-1}. The flat punch was recorded during the compression with the use of an optical microscope by Keyence (VHX-5000) at 400× magnification and a frequency of 15 Hz. The displacements of interest were estimated in a post-processing step by utilizing the digital image correlation software by Correlated Solutions (VIC-2D). The corresponding results are summarized in Section 5.4.

5. Results and discussion

5.1. Elastic properties of the tetrachiral metamaterial

Using the discrete homogenization analysis method (Section 2.3.1), we compute the elastic and shear moduli as well as the coupling coefficients of Eq. (4) for the tetrachiral lattice of Fig. 2. The resulting analytical expressions for the normal and shear modulus are given as a function of the modulus of the base material

E_s as follows:

$$E_x = E_y = \frac{4E_s}{\eta(8sc^4\eta^2 + 2c^5\eta^2 - 9c^2s\eta^2 - 8c^3\eta^2 - 4c^2s + s\eta^2 + 4c^3 + 6c\eta^2 + 2s)}$$

$$G_{xy} = \frac{2E_s}{\eta(-4sc^4\eta^2 + 4c^3\eta^2 + 2c^2s + s\eta^2 - 4c^3 - 2c\eta^2 - s + 4c)},$$

(18)

The corresponding expressions for the coupling coefficients of Eq. (3) are computed as follows:

$$\chi_{xy,x} = \frac{-8s^2c^3\eta^2 + (6\eta^2 - 8)sc^2 + 2s^2(\eta^2 + 2)c + (-2\eta^2 + 2)s}{2c^5\eta^2 + 8sc^4\eta^2 + (4 - 8\eta^2)c^3 - (9\eta^2 + 4)sc^2 + 6c\eta^2 + s(\eta^2 + 2)}, \quad \chi_{xy,y} = -\chi_{xy,x}$$

$$\chi_{x,xy} = \frac{4s^2c^3\eta^2 + sc^2(-3\eta^2 + 4) - s^2c(\eta^2 + 2) + s(\eta^2 - 1)}{4sc^4\eta^2 - 4c^3\eta^2 - 2c^2s - s\eta^2 + 4c^3 + 2c\eta^2 + s - 4c}, \quad \chi_{y,xy} = -\chi_{x,xy}$$

(19)

In Fig. 3c, we provide the dependence both of the normal and of the shear modulus summarized in Eq. (18), as a function of the angular arrangement of the unit-cell for a slenderness value $\eta = 10$. The results indicate that increasing the unit-cell angle θ leads to a lower effective normal modulus and to an increased shear stiffness. What is more, the normal to shear coupling coefficient $\chi_{x,xy}$ decreases for a lattice angle of 20° with respect to an angle of 5° by approximately 50% (Fig. 3d). Contrariwise, the $\chi_{xy,x}$ coefficient increases upon increasing lattice angle, remaining however almost an order of magnitude lower than the $\chi_{x,xy}$ coefficient (Fig. 3d).

In Fig. 5, we present the dependence of the effective normal and shear moduli (Fig. 5 left), as well as of the normal to shear coupling coefficients (Fig. 5 right) on the lattice slenderness ratio η for a given lattice angle θ, which has been set to 15° and $E_s = 1$. In Fig. 5, we depict the discrete homogenization results with continuous and dotted lines, while we use red dots for the full-scale finite element computation results. The discrete and the continuous homogenization results of Fig. 5 lie in close agreement for all mechanical parameters and slenderness ratio values η.

Comparing Fig. 3c with the left subplot of Fig. 5, we note that the inner element slenderness η has a more prominent effect on the normal and shear moduli than the angular arrangement of the unit-cells. In particular, both the normal E_x and the shear material modulus G_{xy} decrease in a hyperbolic manner upon increasing element slenderness η, with low and high slenderness effective properties to differ by orders of magnitude. Contrariwise, the normal to shear coupling coefficients $\chi_{xy,x}$ and $\chi_{x,xy}$ remain either practically unaffected ($\chi_{x,xy}$) or slightly increase for higher η values. As of the lattices' tetragonal symmetry [34], the corresponding y-axis related coupling coefficients are equal and opposite to the x-axis ones, so that $\chi_{xy,y} = -\chi_{xy,x}$ and $\chi_{y,xy} = -\chi_{x,xy}$; a result that has been verified for the analytical formulas of Eq. (19).
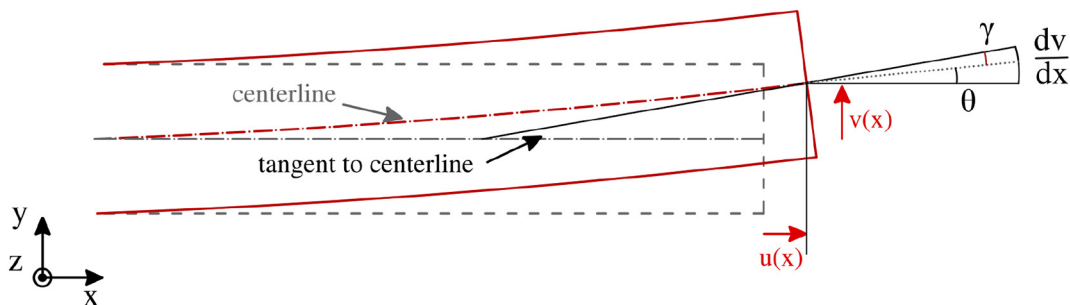

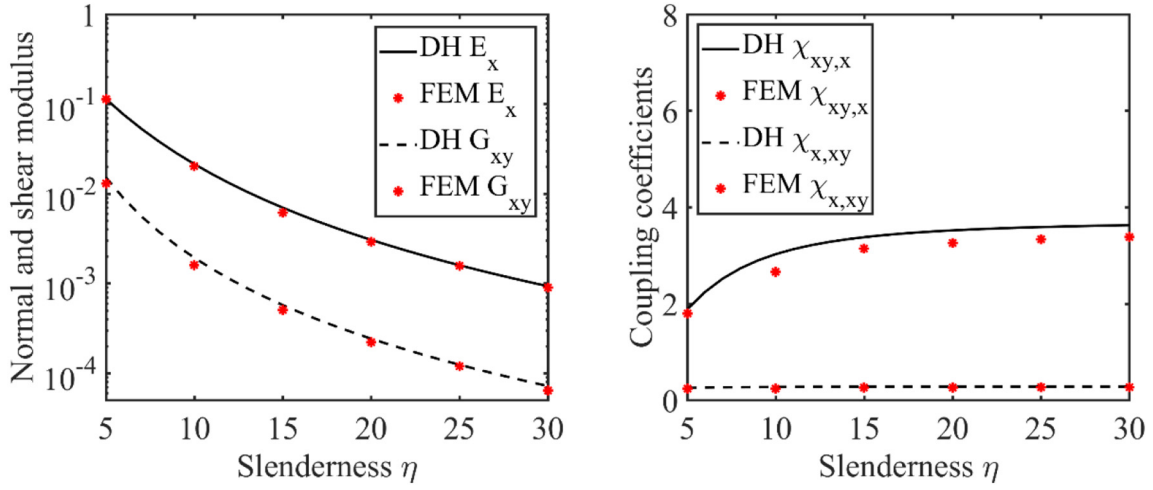**Fig. 4.** Beam kinematics accounting for Timoshenko mechanics.

Fig. 5. Normal and shear modulus E_x, G_{xy} (a) and coupling coefficients $\chi_{xy,x}$ and $\chi_{x,xy}$ (b), as a function of the unit-cell element slenderness η for the tetrachiral lattice structure of Fig. 2 with $\theta = 15°$.

5.2. Deformation and equilibrium mechanics of cantilever beam structures with an inner normal to shear strain coupling

According to the extended Timoshenko-mechanics based theory of Section 3.1, the deflection of an anisotropic cantilever beam for the case of the concurrent action of a distributed load q and of a normal load N_l (Fig. 6) is given in the form of a closed-form expression, as follows:

$$v(x) = \frac{1}{G_{xy}A}\left(qlx - qx^2/2 + \frac{S_{31}}{S_{33}}N_l x\right) + \frac{1}{E_x I_z}\left(-\frac{ql^2 x^2}{4} + \frac{qlx^3}{6} - \frac{qx^4}{24}\right) \quad (20)$$

while the normal displacement field as:

$$u(x) = \frac{1}{E_x A}\left(N_l x + \frac{S_{13}}{S_{11}}\left(qlx - q\frac{x^2}{2}\right)\right) \quad (21)$$

The deflection $v(x)$ of Eq. (20) simplifies to the well-known cantilever beam tip deflection of classical beam theories ($v(l) = -\frac{ql^4}{8E_x I_z}$) upon a distributed load q, if the shear and normal to shear coupling constitutive contributions are to be neglected. Using Eq. (20), we compute the necessary end-force N_l for the end tip of the cantilever to be equilibrated (v

(l) = 0), as follows:

$$N_l = \frac{S_{33}G_{xy}A}{S_{31}l}\left(\frac{ql^4}{8E_x I_z} - \frac{ql^2}{2G_{xy}A}\right) = \frac{E_x A}{\chi_{xy,x}l}\left(\frac{ql^4}{8E_x I_z} - \frac{ql^2}{2G_{xy}A}\right) \quad (22)$$

In complete analogy, we obtain for the case of point load F at the end of the cantilever (Fig. 6), the following expression for the normal force N_l:

$$N_l = \frac{A}{S_{31}l}\left(\frac{Fl^3}{3E_x I_z} - \frac{Fl}{G_{xy}A}\right) = \frac{E_x A}{\chi_{xy,x}l}\left(\frac{Fl^3}{3E_x I_z} - \frac{Fl}{G_{xy}A}\right) \quad (23)$$

5.3. Numerical validation

We load the cantilever beam structure of Section 3.2 independently once with a distributed load q and once with a point load F (Fig. 6). For a concentrated load of $F = 0.1\,KN$, we compute a normal traction force magnitude of $N_l = 1.77\,KN$ to equilibrate the beam end tip deflection using Eq. (23). The bending deflection due to F amounts to $v^F(l) = 7.34\,mm$ (downwards). Accordingly, we compute the bending deflection created by the normal traction force to be $v_{N_l}(l) = -7.25\,mm$ pointing upwards, in a counter-clockwise rotational direction, thus opposite to the bending deformation created by F. Fig. 7b provides a schematic representation of the deformed specimen structure, created
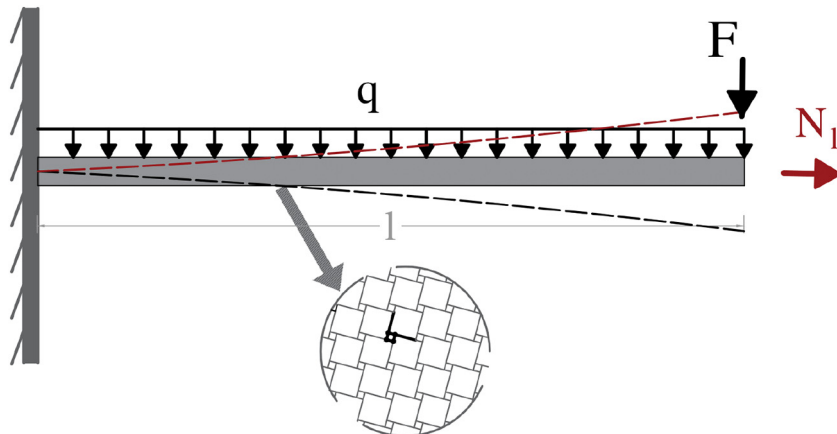

Fig. 6. Cantilever beam architected with a tetrachiral unit cell (Fig. 2) and a constitutive law with a normal to shear strain coupling.
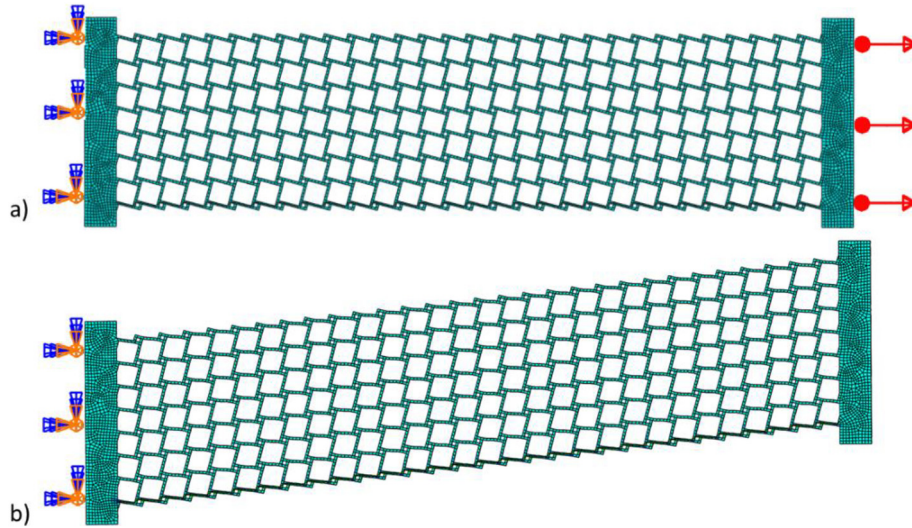
Fig. 7. Numerical model of a metamaterial beam structure architected with tetrachiral unit-cells, clamped at its left end, end normally loaded at its right end (a). Its deformed configuration after the application of an end normal load N_l is depicted in (b).

solely by the application of the normal load N_l. The values exhibit a relative difference of $| v^F(l) - v^{N_l}(l) | / v^F(l) = 1\%$, suggesting a very good agreement of the analytical formula predictions of Section 5.2 with the numerical results.

In an analogous manner we compute the normal force required to equilibrate the cantilever beam structure of Section 3.2 when subject to a distributed load $q = 0.01 \, KN/mm$. Using Eq. (22), we obtain a normal load value of $N_l = 13.64 \, KN$. The bending deflection created by the distributed load q is $v^q(l) = 60.8 \, mm$. Applying the traction load N_l at the end of the cantilever yields an upward, opposite direction deflection of $v^{N_l}(l) = -58.9 \, mm$. Its absolute magnitude lies in very close agreement with the one created by the distributed load ($| v^q(l) - v^{N_l}(l) | / v^q(l) = 3\%$), counterbalancing the created bending deflection. The results are summarized in Table 2.

5.4. Experimental validation

We subsequently analyze the bending displacement profile created by the application of normal forces at the tip of the architected tetrachiral structure. Using the analytical expressions of Eqs. (20) and (21) for the displacement profiles and setting the terms related to the external bending loads to zero ($q = 0$), we obtain for the horizontal and vertical displacement field the following expressions:

$$
\left.
\begin{aligned}
u(x) &= \frac{N_l x}{E_x A} \\
v(x) &= \frac{S_{31}}{S_{33}} \frac{N_l x}{G_{xy} A}
\end{aligned}
\right\}
\Rightarrow v(x)/u(x) = \left(\frac{S_{31}}{S_{33}} \frac{N_l x}{G_{xy} A} \right) / \left(\frac{N_l x}{E_x A} \right) = S_{31} \cdot E_x
$$

$$
= \frac{S_{31}}{S_{11}} = \chi_{xy,x} \tag{24}
$$

where in Eq. (24), the definitions of Eqs. (3) and (4) have been employed. Eq. (24) suggests that the ratio of displacements $v(x)/u(x)$ is independent of the magnitude of the normal force applied and of

the position x of interest, being a constant. The displacement ratio is equal to $\chi_{xy,x}$, which is a characteristic parameter for the cantilever structure's normal to shear strain structural behaviour.

In Fig. 8, we experimentally investigate the bending displacement profile created upon the application of normal forces, making use of cantilever beam specimens architected with tetrachiral elements (Fig. 8a, b). In Fig. 8c, the resulting vertical bending deflection $v(l)$ at the centerline of the cantilever tip is presented as a function of the horizontal displacement $u(l)$, throughout the loading time. In Fig. 8d we provide the mean displacement ratio based on the slope of Fig. 8c.

We note that the ratio of the tip bending deflection to the tip normal displacement (Fig. 8d) is in close agreement with the analytical predictions of Eq. (24) for the design specifications of Section 4. In particular, the ratio of the bending to the horizontal displacement v/u has been computed to be $v/u = 1.97 \pm 0.15$, providing a mean value of 1.97 coupling coefficient $\chi_{xy,x}$. The slope variance is to be primarily attributed to the variance of the element slenderness ratio $\eta = 6.5 \pm 0.5$ in the fabrication process (Section 4). It is to note that the bending deflection v is higher than the structures' normal displacement, so that a rather minimal normal strain of 0.5% ($u = 3\mu m$) induces a bending deflection that is approximately 1% ($v \approx 6\mu m$) of the cantilever beams' length. We provide a video of the cantilever deformation upon normal loading in the form of complementary material.

5.5. Discussion

For the vast majority of common engineering materials, such as metals, polymers and rubbers, uniaxial normal loads cause deformations within the direction of the load application [47,48]. As such, the material's bending and normal deformations can be well separated, so that changes in its bending or normal displacement field take place independently under small strains.

Coupling the material's normal and bending deformation modes provides an additional design degree of freedom. In such a design

Table 2
End tip displacements of the cantilever beam upon the action of point or distributed bending loads concurrently with a normal end force.

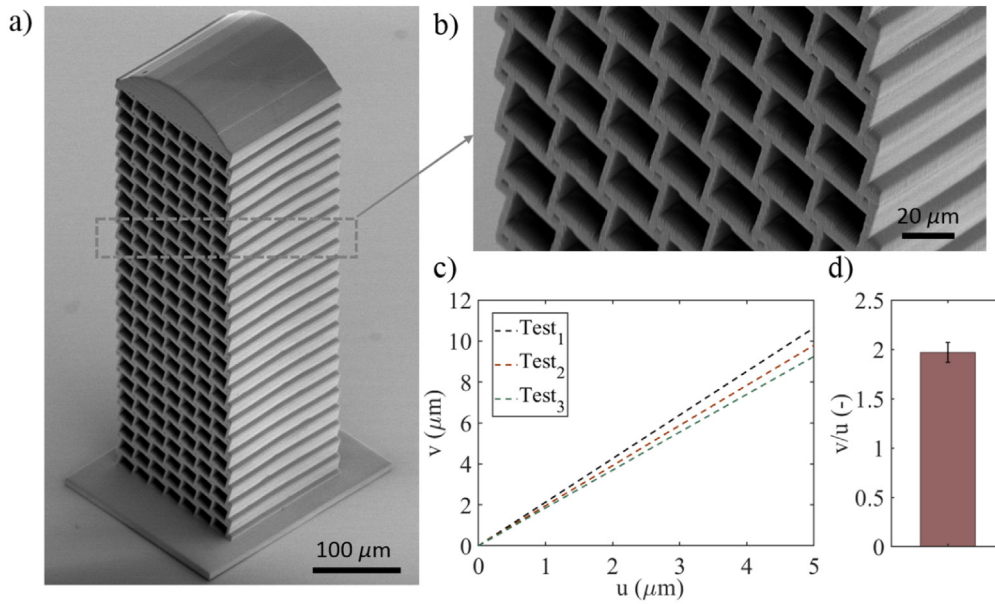| Load	$F \mid q \, (KN|KN/mm)$	$N_l \, (KN)$	$v_{F/q} \, (mm)$	$v_{N_l} \, (mm)$	$\frac{(v_{F/q} - v_{N_l})}{v_{F/q}} (\%)$
Point	0.1	1.77	7.34	−7.25	1
Distributed	0.01	13.64	60.8	−58.9	3

Fig. 8. Micro-architected cantilever beam structure of a length of $600\mu m$ (a) architected with tetrachiral unit cells of a slenderness ratio $\eta = 6.5 \pm 0.5$. The relation of the centerline end-tip bending deflection $v(x)$ to the horizontal displacement is linear for each of the 3 specimens tested (c), with a slope of 1.97 ± 0.15 (d).

domain, bending effects can be modulated by normal loads and vice versa. For the coupling of the material's mechanics to become feasible, a non-isotropic constitutive material behaviour is required, so that the off-diagonal terms of Eq. (2) are non-zero. However, anisotropy does not uniquely entail a fully populated constitutive matrix [33]. For the two-dimensional constitutive behaviour of Eq. (2), several anisotropic inner material designs can be identified with a decoupled effective normal and bending behaviour, indicative examples being artificial materials architected with square or re-entrant hexagonal unit-cells [34].

However, when anisotropy is combined with chirality, as in the case of a metamaterial that is architectured with the tetrachiral unit-cell structures of Fig. 2, bulk deformations are coupled to rotations. As a result, normal forces induce lateral bending displacements, while bending loads can be exerted to trigger contraction or extension. For the cantilever beam of Fig. 6, the application of a purely axial load N_l creates a horizontal and a vertical displacement field $u(x)$ and $v(x)$ (Section 5.2) which are related by the normal to shear load coupling coefficient $\chi_{xy,x}$ (Section 5.4). The latter varies within rather narrow bounds for the different unit-cell designs (different θ Fig. 3d and η values Fig. 5b), contrary to the material's normal and shear resistance, which can be tuned to adjust the extensional and bending strength of the cantilever by orders of magnitude (Fig. 5a).

The mechanical behaviour arising from the constitutive coupling among normal and shear strains can be effectuated both at a macro (Section 5.3) and at a microscale (Section 5.4). However, classical bending theories do not suffice to characterize a mechanical response of the kind, as they a-priori assume simplified, uncoupled kinematics [56]. As a result, an enhanced constitutive formulation is required for the coupled mechanics to be captured (Sections 3.1, 5.2). Using the tetrachiral unit-cell structure of Fig. 2, tensile normal forces need to be applied, in order to counterbalance the end tip bending deflection of the architected cantilever structure (Section 5.2). The sign and the magnitude of normal load to be applied, directly relates to the normal to shear coupling coefficient $\chi_{xy,x}$ (which is strictly positive for the lattice designs of Fig. 5), a parameter that is controlled by the unit-cell design and can be optimized to meet certain objectives for the homogenized response; an analysis which exceeds the scope of the current work. Moreover, the applied normal load is proportional to the length of the architected beam structure, so that higher beam lengths require increased normal forces to equilibrate (Eqs. (22)–(23)).

6. Conclusions

Overall, the current work has analysed the potential of structures with a non-isotropic and chiral inner material architecture to balance bending loads though tensile loads, harnessing their inherent coupling of normal and bending deformations. To that scope, the enhanced formulation required for the description of their coupled normal and bending response has been derived in the context of beam mechanics, starting from first principles. Thereupon, closed-form parametric expressions have been elaborated for the equilibration of cantilever beam structures under concentrated and distributed bending loads. The analytical results have been complemented by dedicated numerical and experimental investigations. The results suggest that the coupling of normal and shear deformations is a constitutive material behaviour that can be used as a primal structural deformation control mechanism. We aspire that the current work provides the basis, not only for the analysis and design of beam structures of the kind, but also for the engineering of a wide range of structures, such as plates and domes, with an inherently enhanced kinematic behaviour, which harnesses inner normal to shear couplings to balance macroscopic, externally applied loads.

Nomenclature

ρ^*	relative density
η	slenderness ratio
L	lattice element length
t	element thickness
θ	lattice angle
λ_i	lattice periodicity vectors
$\boldsymbol{\varepsilon}$	strain tensor
$\boldsymbol{\sigma}$	stress tensor
$\mathbf{S}$	compliance tensor
$\mathbf{C}$	stiffness tensor
E	normal modulus
G	Shear modulus
ν	Poisson's ratio
χ	coupling coefficients
$\mathbf{F}^b$	lattice forces
$\mathbf{M}$	lattice moments
$\mathbf{v}_f$	velocity fields
$\mathbf{w}$	rotation fields
δ	tessellation index

g	Jacobian
ϕ_x	beam axial twist
u	beam axial displacement
v	beam deflection
A	beam section area
N	beam axial force
V	beam shear force
M_z	beam bending moment
I_z	moment of inertia
q	beam distributed load
F	beam concentrated load
N_I	beam axial force

Supplementary data to this article can be found online at https://doi.org/10.1016/j.matdes.2020.108520.

Declaration of competing interests

The authors declare that they have no known competing financial interests or personal relationships that could have appeared to influence the work reported in this paper.

CRediT authorship contribution statement

N. Karathanasopoulos: Conceptualization, Methodology, Formal analysis, Writing - original draft.**F. Dos Reis:**Methodology, Validation. **M. Diamantopoulou:**Investigation, Validation.**J.-F. Ganghoffer:** Validation.

Acknowledgements

Data availability

The raw data required to reproduce the experimental findings of the work are available to download from https://karathanasopoulos.gr/software/

References

[1] Y. Liu, X. Zhang, Metamaterials: a new frontier of science and technology, Chem. Soc. Rev. 40 (2011) 2494–2507.
[2] T.J. Cui, D.R. Smith, R.P. Liu, Metamaterials: Theory, Design and Applications, Springer, 2010.
[3] K. Liu, T. Zegard, P.P. Pratapa, G.H. Paulino, Unraveling tensegrity tessellations for metamaterials with tunable stiffness and bandgaps, J. Mech. Phys. Solids 131 (2019) 147–166.
[4] D.R. Smith, J.B. Pendry, Homogenization of metamaterials by field averaging, J. Opt. Soc. Am. B 23 (3) (2006) 391.
[5] Hao-Wen Dong, Sheng-Dong Zhao, Yue-Sheng Wang, Chuanzeng Zhang, Topology optimization of anisotropic broadband double-negative elastic metamaterials, J. Mech. Phys. Solids 105 (2017) 54–80.
[6] Y. Liu, H. Hu, A review on auxetic structures and polymeric materials, Sci. Res. Essays 5 (10) (2010) 1052–1063.
[7] X. Zhu, L. Xu, X. Liu, J. Xu, P. Hu, Z.-D. Ma, Theoretical prediction of mechanical properties of 3D printed Kagome honeycombs and its experimental evaluation, Proceedings of the Institution of Mechanical Engineers, Part C: J. of Mech. Eng. Sc. 233 (18) (2019) 6559–6576.
[8] M.S. Rad, H. Hatami, Z. Ahmad, A.K. Yasuri, Analytical solution and finite element approach to the dense re-entrant unit cells of auxetic structures, Acta Mech. 230 (6) (2019) 2171–2185.
[9] T. Tancogne-Dejean, N. Karathanasopoulos, D. Mohr, Stiffness and strength of hexachiral honeycomb-like metamaterials, ASME. J. Appl. Mech. 86 (11) (2019) 111010.
[10] M. Mosby, K. Matouš, Computational homogenization at extreme scales, Extreme Mechanics Letters 6 (2016) 68–74.
[11] M. Tabatabaei, D. Le, S.N. Atluri, Nearly exact and highly efficient elastic-plastic homogenization and/or direct numerical simulation of low-mass metallic systems with architected cellular microstructures, J. Mech. Mater. Struct. 12 (5) (2017).
[12] L. Kaczmarczyk, C.J. Pearce, N. Bicanic, Studies of microstructural size effect and higher-order deformation in second-order computational homogenization, Comp. and Struct. 88 (23–24) (2010) 1383–1390.
[13] F. Dos Reis, J.F. Ganghoffer, Construction of micropolar continua from the asymptotic homogenization of beam lattices, Comp. and Struct. 112-113 (2012) 354–363.
[14] F. Dos Reis, J.F. Ganghoffer, Equivalent mechanical properties of auxetic lattices from discrete homogenization, Comp. Mat. Sc. 51 (1) (2012) 314–321.
[15] G.N. Greaves, A.L. Greer, R.S. Lakes, T. Rouxel, Poisson's ratio and modern materials, Nat. Mater. 10 (2011) 823–838.
[16] Y. Prawoto, Seeing auxetic materials from the mechanics point of view: a structural review on the negative Poisson's ratio, Comput. Mater. Sci. 58 (2012) 140–153.
[17] K.E. Evans, A. Alderson, Auxetic materials: functional materials and structures from lateral thinking! Adv. Mater. 12 (2000) 617–628.
[18] J.N. Grima, L. Mizzi, K.M. Azzopardi, R. Gatt, Auxetic perforated mechanical metamaterials with randomly oriented cuts, Adv. Mater. 28 (2016) 385–389.
[19] X. Ren, J. Shen, P. Tran, T.D. Ngo, Y.M. Xie, Design and characterisation of a tuneable 3D buckling-induced auxetic metamaterial, Mater. Des. 139 (2018) 336–342.
[20] R. Brighenti, A. Spagnoli, M. Lanfranchi, F. Soncini, Nonlinear deformation behaviour of auxetic cellular materials with re-entrant lattice structure, Fatigue Fract. Engng. Mater. Struct. 39 (2016) 1460–2695.
[21] P.S. Theocaris, G.E. Stavroulakis, P.D. Panagiotopoulos, Negative Poisson's ratios in composites with star-shaped inclusions: a numerical homogenization approach, Arch. Appl. Mech. 67 (4) (1997) 274–286.
[22] K.E. Evans, B.D. Caddock, M.J. Nobes, Microporous materials with negative Poisson's ratios. II. Mechanisms and interpretation, J. of Phys. 22 (1989) 1883–1887.
[23] N. Gaspar, X.J. Ren, C.W. Smith, J.N. Grima, K.E. Evans, Novel honeycombs with auxetic behaviour, Acta Mater. 53 (8) (2005) 2439–2445.
[24] J.N. Grima, R. Gatt, N. Ravirala, A. Alderson, K.E. Evans, Negative Poisson's ratios in cellular foam materials, Mater. Sci. Eng. A 423 (1) (2006) 214–218.
[25] H. Yang, L. Ma, Multi-stable mechanical metamaterials with shape-reconfiguration and zero Poisson's ratio, Mater. Des. 152 (2018) 181–190.
[26] R.S. Kumar, D.L. McDowell, Multifunctional design of two-dimensional cellular materials with tailored mesostructure, Int. J. Solids and Struct. 46 (14) (2009) 2871–2885.
[27] J.N. Grima, L. Oliveri, D. Attard, B. Ellul, R. Gatt, G. Cicala, G. Recca, Hexagonal honeycombs with zero Poisson's ratios and enhanced stiffness, Adv. Eng. Mater. 12 (2010) 855–862.
[28] Y.H. Zhang, X.M. Qiu, D.N. Fang, Mechanical properties of two novel planar lattice structures, Int. J. of Solids and Struct. 45 (13) (2008) 3741–3768.
[29] X. Zheng, H. Lee, T.H. Weisgraber, M. Shusteff, J. DeOtte, E.B. Duoss, J.D. Kuntz, M.M. Biener, Q. Ge, J.A. Jackson, S.O. Kucheyev, N.X. Fang, C.M. Spadaccini, Ultralight, ultrastiff mechanical metamaterials, Science 344 (6190) (2014) 1373–1377.
[30] S. Xu, J. Shen, S. Zhou, X. Huang, Y.M. Xie, Design of lattice structures with controlled anisotropy, Mater. Des. 93 (2016) 443–447.
[31] M. Tabatabaei, S.N. Atluri, Ultralight cellular composite materials with architected geometrical structure, Compos. Struct. 196 (2018) 181–198.
[32] L.R. Meza, S. Das, J.R. Greer, Strong, lightweight, and recoverable three-dimensional ceramic nanolattices, Science 345 (6202) (2014) 1322–1326.
[33] M.L.M. François, L. Chen, M. Coret, Elasticity and symmetry of triangular lattice materials, Int. J. of Solids and Struct. 129 (2017) 18–27.
[34] N. Karathanasopoulos, F. Dos Reis, H. Reda, J.-F. Ganghoffer, Computing the effective bulk and normal to shear properties of common two-dimensional architectured materials, Comput. Mater. Sci. 154 (2018) 284–294.
[35] X.Y. Yang, X. Huang, J.H. Rong, Y.M. Xie, Design of 3d orthotropic materials with prescribed ratios for effective Youngs moduli, Comput. Mater. Sci. 67 (2013) 229–237.
[36] N. Karathanasopoulos, H. Reda, J.-F. Ganghoffer, Designing two-dimensional metamaterials of controlled static and dynamic properties, Comput. Mater. Sci. 138 (2017) 323–332.
[37] L.D. Peel, Exploration of high and negative Poisson's ratio elastomer-matrix laminates, Phys. Status Solidi 1003 (3) (2007) 988–1003.
[38] Y. Wu, et al., Three-dimensionally bonded spongy graphene material with super compressive elasticity and near-zero Poisson's ratio, Nat. Commun. 6 (6141) (2015).
[39] H. Reda, N. Karathanasopoulos, K. Elnady, J.F. Ganghoffer, H. Lakiss, Mechanics of metamaterials: an overview of recent developments, Advances in Mechanics of Microstructured Media and Structures, 87, Springer 2018, p. 273:296.
[40] A.S. Phani, J. Woodhouse, N.A. Fleck, Wave propagation in two-dimensional periodic lattices, J. Acoust. Soc. Am. 119 (2006).
[41] S. Gonella, M. Ruzzene, Analysis of in-plane wave propagation in hexagonal and re-entrant lattices, J. Sound Vib. 312 (2008) 125–139.
[42] A. Bacigalupo, M.L. De Bellis, Auxetic anti-tetrachiral materials: equivalent elastic properties and frequency band-gaps, Compos. Struct. 131 (2015) 530–544.
[43] H. Reda, N. Karathanasopoulos, J.F. Ganghoffer, H. Lakiss, Wave propagation characteristics of periodic structures accounting for the effect of their higher order inner material kinematics, J. Sound Vib. 431 (2018) 265–275.
[44] R. Zhu, Y.Y. Chen, Y.S. Wang, G.K. Hu, G.L. Huang, A single-phase elastic hyperbolic metamaterial with anisotropic mass density, J. Acoust. Soc. Am. 139 (2016) 3303–3310.
[45] R. Zhu, H. Yasuda, G.L. Huang, J. Yang, Kirigami-based elastic metamaterials with anisotropic mass density for subwavelength flexural wave control, Sci. Rep. 8 (2016) 483.
[46] C. Shen, Y. Xie, S. Yangbo, W. Ni, W. Wang, S. Cummer, Y. Jing, Broadband acoustic hyperbolic Metamaterial, Phys. Rev. Lett. 115 (254301) (2015).
[47] X.N. Liu, G.L. Huang, G.K. Hu, Chiral effect in plane isotropic micropolar elasticity and its application to chiral lattices, Journal of the Mechanics and Physics of Solids 60 (11) (2012) 1907–1921.
[48] C. Coulais, As the extension, so the twist, Science 358 (2017) 994–995.
[49] A. Alderson, K.L. Alderson, D. Attard, K.E. Evans, R. Gatt, J.N. Grima, W. Miller, N. Ravirala, C.W. Smith, K. Zied, Elastic constants of 3-, 4- and 6-connected chiral and

anti-chiral honeycombs subject to uniaxial in-plane loading, Compos. Sci. Technol. 70 (7) (2010) 1042–1048.

[50] H. Ebrahimi, D. Mousanezhad, H. Nayeb-Hashemi, J. Norato, A. Vaziri, 3D cellular metamaterials with planar anti-chiral topology, Mater. Des. 145 (2018) 226–231.

[51] D. Prall, R.S. Lakes, Properties of a chiral honeycomb with a Poisson's ratio of −1, Intern. J. of Mech. Sc. 39 (3) (1997) 305–314.

[52] W. Zhang, R. Neville, D. Zhang, F. Scarpa, L. Wang, R. Lakes, The two-dimensional elasticity of a chiral hinge lattice metamaterial, Int. J. of Solids and Struct. 141-142 (2018) 254–263.

[53] A. Bacigalupo, L. Gambarotta, Homogenization of periodic hexa- and tetrachiral cellular solids, Compos. Struct. 116 (1) (2014) 461–476.

[54] H.G. Kwak, J.K. Son, Span ratios in bridges constructed using a balanced cantilever method, Constr. Build. Mater. 18 (10) (2004) 767–779.

[55] G.L. Balázs, G. Farkas, T. Kovács, Reinforced and prestressed concrete bridges, Innovative Bridge Design Handbook, Butterworth-Heineman, ISBN: 9780128000588 2016, pp. 213–246.

[56] A. Bazoune, Y.A. Khulief, N.G. Stephen, Shape functions of three-dimensional Timoshenko beam elements, J. Sound Vib. 259 (2) (2003) 473–480.

[57] O.C. Zienkiewicz, R.L. Taylor, D. Fox, The Finite Element Method for Solid and Structural Mechanics, Butterworth-Heinemann, 2014.

[58] T. Tancogne-Dejean, M. Diamantopoulou, M. Gorji, C. Bonatti, D. Mohr, 3D plate-lattices: an emerging class of low-density Metamaterial exhibiting optimal isotropic stiffness, Adv. Mater. 30 (2018) 1803334.